WILEY

RESEARCH ARTICLE `OPEN ACCESS`

Continuous Curvature Path Planning for Headland Coverage With Agricultural Robots

Gonzalo Mier[1] | Rick Fennema[1] | João Valente[2] | Sytze de Bruin[1]

[1]Laboratory of Geo-Information Science and Remote Sensing, Wageningen University & Research, Wageningen, The Netherlands | [2]Centre for Automation and Robotics (CAR), Spanish National Research Council (CSIC), Madrid, Spain

Correspondence: Gonzalo Mier (gonzalo.miermunoz@wur.nl)

ABSTRACT

We introduce a methodology for headland coverage planning for autonomous agricultural robot systems, which is a complex problem often overlooked in agricultural robotics. At the corners of the headlands, a robot faces the risk to cross the border of a field while turning. Though potentially dangerous, current papers about corner turns in headlands do not tackle this issue. Moreover, they produce paths with curvature discontinuities, which are not feasible by non-holonomic robots. This paper presents an approach to strictly adhere to field borders during the headland coverage, and three types of continuous curvature turn planners for convex and concave corners. The turning planners are evaluated in terms of path length and uncovered area to assess their effectiveness in headland corner navigation. Through empirical validation, including extensive tests on a coverage path planning benchmark as well as real-field experiments with an autonomous robot, the proposed approach demonstrates its practical applicability and effectiveness. In simulations, the mean coverage area of the fields went from 94.73%, using a constant offset around the field, to 97.29% using the proposed approach. Besides providing a solution to the coverage of headlands in agricultural automation, this paper also extends the covered area on the mainland, thus increasing the overall productivity of the field.

1 | Introduction

In recent years, the role of agricultural automation in transforming farming methodologies has been crucial. The advent of autonomous agricultural robot systems (Figure 1) has marked a significant advancement in agriculture, facilitating the enhancement of operational efficiency and crop yields (Oliveira et al. 2021). These systems autonomously and precisely traverse agricultural fields, executing tasks like harvesting (Rahman et al. 2019; Nørremark et al. 2022) and spraying (Spekken and de Bruin 2013) as required by the specific location.

Agricultural fields are generally categorized into two main sections: the mainland, that is, the primary area of operations, and the headlands, predominantly used for turning between the swaths covering the mainland. The optimization of mainland coverage has been the primary focus of many studies (Höffmann, Patel, and Büskens 2023a, 2023b), whereas the headland areas that are crucial for comprehensive field management, have been much less studied.

Headlands are typically formed as concentric tracks, their number and dimensions varying according to the operational requirements and the space needed for tractor maneuvers

---

FIGURE 1 | The AgBot 5.115T2 of the company AgXeed B.V (The Netherlands) with a mounted Amazone Cenius 3000 Super cultivator combined with a seed drill.

(Paraforos et al. 2018). Research on headland management has mainly concentrated on optimizing turns between swaths, employing various strategies like route planning to minimize nonworking time (Bochtis and Vougioukas 2008), selecting headland turning types to decrease expenses (Spekken et al. 2015), and path planners for turns in the headland avoiding getting out of the field when the tractor is equipped with mounted implements (Trendafilov et al. 2023). These path planners aim to go from one point to another known point (Nobari et al. 2019). However, comprehensive approaches for effective between-track maneuvers on the headlands and particularly maneuvers along corners remain sparse.

To date, most turning planners rely on circular segments (Nilsson and Zhou 2020; Jeon et al. 2021), or noncontinuous-curvature curves (PourArab et al. 2023), such as Dubins (Dubins 1957) or Reeds-Shepp (Reeds and Shepp 1990) paths, comprising sequences of circles and straight lines. These paths, however, are unsuitable for non-holonomic robotic systems owing to sudden directional changes. To mitigate this issue, (Fraichard and Scheuer 2004) suggested an adaptation of Reeds-Shepp's curve using clothoids for smoother transitions. While this has been for swath-to-swath turns in agricultural fields (Sabelhaus and Röben 2013), it has not been used for within-headland navigation. Also Nonuniform Rational B-Splines (NURBs) have been proposed (Höffmann et al. 2022) for smoother headland paths, focusing solely on forward movement. However, these do not effectively cover the corners as the method focuses on path planning around the headland rather than the coverage of it. For corner coverage in headlands, Jeon et al. (2021) introduced a back-and-forth maneuver, neglecting physical constrains on speed of curvature changes.

While some studies go beyond simply considering maximum curvature and operational width (e.g., Jeon et al. 2021), they have so far disregarded the dimensions of both the tractor and the implement for preventing overstepping field boundaries during turns. Crossing field boundaries unexpectedly poses safety risks to machinery, external property, and farmers. To our knowledge

and as shown in Table 1, our work is the first that ensures field borders not to be crossed, thanks to a more complete representation of the robot and implement geometry. Additionally, our approach maximizes field coverage by utilizing backward movements while maintaining continuous curvature along the paths. As previously mentioned, noncontinuous curvature paths are unfeasible for non-holonomic vehicles, such as tractors, which may explain why (PourArab et al. 2023) did not test their algorithm in a real environment, and (Jeon et al. 2021) experiments relied on a human driver, instead of autonomous robots.

This study builds on existing non-curvature-continuous corner path planners (Jeon et al. 2021), integrating solutions for continuous curvature turns to achieve headland coverage using real-world robotic implementations. The proposed method employs clothoids for generating smooth transitions between intersecting lines (Baykal et al. 1997), a technique commonly used in road alignment, but scarcely in agricultural path planning. We introduce a method for improving the coverage of the headland area while constraining the robot and the attached implement to stay within the field borders. To do so, a minimal safety offset for each border of the field is computed, considering the type of turn and the robot geometry and three types of continuous curvature turns for headland corners. The selection method for the corner turn planner employs two objective functions, that is, path length and the area uncovered.

This paper substantially contributes to the field of headland coverage path planning in agricultural operations, offering the following key advancements.

- **Continuous Curvature Corner Path Planners**: Three different types of corner turn planners (C-type, B-type, and X-type corner turns) are presented. Those corner turn planners are suitable for both convex and concave corners while generating paths with continuous curvature.

- **Method to Constrain the Agricultural Robot to Field Borders**: A thorough analysis is presented, quantifying

Approaches	(Pour Arab et al. (2022))	(Höffmann et al. (2022))	(Jeon et al. (2021))	Our approach
1. Continuous curvature paths	✗	✓	✗	✓
2. Allow reverse movement	✓	✗	✓	✓
3. Support for concave corners	✗[a]	✓	✗	✓
4. Implement not in center of robot	✗	✗	✓	✓
5. Coverage area ≠ Implement area	✗	✗	✗	✓
6. Multiple cost functions	✗	✗	✗	✓
7. Guarantee field borders are not crossed	✗	✗	✗	✓
8. Tested autonomously on real experiment	✗	✗	✗[b]	✓

[a]Concave corners are treated as convex corners, ignoring the field borders.
[b]Using human driver.

the degree to which agricultural implements exceed field borders during corner maneuvers. Additionally, a strategy is provided to mitigate instances of exiting the field borders by offsetting the edges of the border the distance exceeded by the robotic system.

- **Automatic Turn Selection**: The study proposes dual objective functions—area coverage and travel distance—for selecting among C-type, B-type, and X-type corner turns. This systematic evaluation of each turn type against these objectives aims to optimize field coverage and enhance navigation efficiency.

- **Simulated and Real Field Eexperiments**: The methods have been tested in simulation using the (Nilsson and Zhou 2020) benchmark, and on a real field with an autonomous robot. These experiments prove the validity of the proposed methods.

2 | Methods

The proposed algorithm is represented in the block diagram of Figure 2. The inputs of the diagram are the robot data (Section 2.1), the number of headland tracks, and the field shape. The first step to plan the headland coverage path is to collect the corners (Section 2.3) and transform them to a local system (Section 2.4). For each corner, the path to cover the corner is computed, depending if the corner is convex (Section 2.5) or concave (Section 2.6). To avoid overpassing the corner edges, the central path is moved an offset inwards the field. The computation of those offsets is explained on Section 2.7. This paper proposes three planners. Choosing the best planner for each corner requires to define a cost function. In the case of headland coverage, the objective of the turns is to cover the maximum area while driving the shortest path. This trade-off is handled using a sum of normalized cost functions (Section 2.9). After selecting the planners for the corners, the offsets are used to move inwards the field borders (Section 2.8). Finally, the turns are recomputed using the new offsets, and the headland coverage path is obtained by concatenating the turns of each corner (Section 2.8).
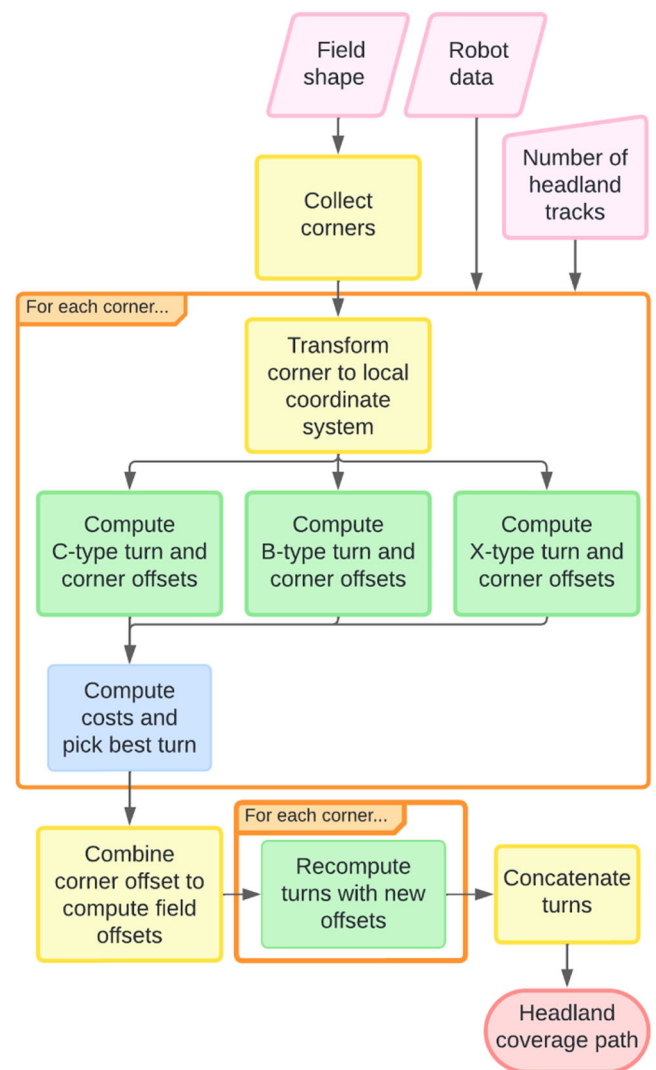
FIGURE 2 | Block diagram of the proposed algorithm. Inputs are drawn in pink, geometric transformations in yellow, corner planners in green, cost functions in blue and output in red.

FIGURE 3 | Autonomous robot, represented by a blue box, equipped with a mounted implement, indicated by a green box. The coverage area of the implement is highlighted in yellow. The centers of both the robot and the implement are marked with symbols "R" (for robot) and "I" (for implement), respectively.

2.1 | Robot Definitions

The geometric model of the robotic system is composed of two rectangular components representing the robot and the implement fixed to it (see Figure 3). The robotic system design assumes symmetry in the motion direction, characterized by three widths: robot's (W_R), implement's (W_I), and overall robotic system's (W_S), the latter being the larger of the former two. The center of the implement is located a distance c_I from the robot's center. When the implement is positioned behind the robot, c_I is negative. The center of the robot also serves as the center of rotation of the robotic system.

The robot and implement lengths are denoted as L_R and L_I, respectively. The positions of the implement front, I_f, and back, I_b, relative to the robot center are $I_f = c_I + \frac{L_I}{2}$ and $I_b = c_I - \frac{L_I}{2}$. The length of the robotic system is thus defined as $L_S = S_f - S_b$, with $S_f = \max(\frac{L_R}{2}, I_f)$ and $S_b = \min(-\frac{L_R}{2}, I_b)$.

The implement operates in two states: "on" (active) and "off" (inactive), with state changes involving a temporal transition. In its active state, the implement covers an area of width W_C and length L_C, centered around the implement's geometrical center. Coverage is achieved when the full working length, L_C, has passed a location. The center of the front part of the implement's coverage area is defined as $C_f = c_I + \frac{L_C}{2}$, and the center of the back part as $C_b = c_I - \frac{L_C}{2}$.

The robot is non-holonomic, meaning that turning is subject to bounded, continuous curvature (κ) and a bounded rate of curvature change (σ), reflecting operational and physical constraints. The maximum curvature, according to the state of the implement, is denoted as $\kappa_{\max}^{on}$ or $\kappa_{\max}^{off}$, while the greatest rate of curvature change is denoted as $\sigma_{\max}$. When active, the implement requires smaller maximum curvature to prevent machinery damage ($\kappa_{\max}^{on} < \kappa_{\max}^{off}$).

This research involves testing on an Agbot robot equipped with an implement (cultivator and seed drill). The dimensions and

TABLE 2 | Dimensions and operational capabilities of the Agbot robot and the Amazone implement (cultivator and seed drill).

Robot width	W_R	3 m
Robot length	L_R	4 m
Implement width	W_I	3.15 m
Implement length	L_I	3.6 m
Coverage width of implement	W_C	3 m
Coverage length of implement	L_C	3 m
Implement center offset	C_I	−3.8 m
Maximum curvature with implement off	$\kappa_{\max}^{off}$	0.5 m^{-1}
Maximum curvature with implement on	$\kappa_{\max}^{on}$	0.05 m^{-1}
Maximum curvature change rate	$\sigma_{\max}$	0.1 m^{-2}

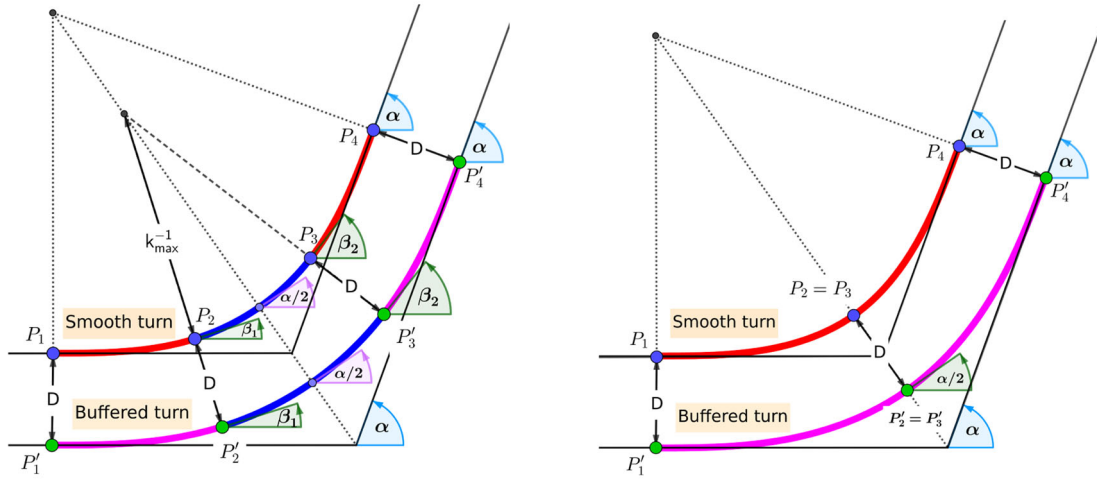operational capabilities of the robot-implement combinations are summarized in Table 2.

2.2 | Smooth Turns

A smooth turn (see Figure 4) is a turn without curvature discontinuities. To transition between two points with a smooth turn, clothoids are used. Clothoids, also known as Euler spirals, are defined by linearly changing curvatures along their length, making smooth transitions from straight to curved paths and vice versa, thus avoiding curvature discontinuities. A clothoid is described by the following equations (Fraichard and Scheuer 2004):

$$\kappa_t^\eta = t\kappa_{\max}, \tag{1}$$

$$\theta_t^\eta = \frac{(t\kappa_{\max})^2}{2 * \sigma}, \tag{2}$$

$$x_t^\eta = \sqrt{\frac{\pi}{\sigma}} C_f\left(\sqrt{\frac{(t\kappa_{\max})^2}{\pi * \sigma}}\right), \tag{3}$$

(a) Smooth turns made by two clothoids and one circular segment. Between points P_2 and P_3, the circular segment has κ_{max} curvature.

(b) Smooth turns made by two clothoids. P_2 and P_3 are the same, and the curvature on that point is $\leq k_{max}$, so no circular segment is used.

FIGURE 4 | Smooth turn and buffered turn. Clothoid are indicated in red; circular segments in blue; magenta denotes buffered clothoids. The buffering distance between both turns is always D. Both turns start with angle 0 and end the turn with angle α. From P_1 to P_2 the curvature increases, and from P_3 to P_4 the curvature decreases. As the curve is symmetric, $\alpha = \beta_1 + \beta_2$. (a) Smooth turns made by two clothoids and one circular segment. Between points P_2 and P_3, the circular segment has κ_{max} curvature. (b) Smooth turns made by only two clothoids. P_2 and P_3 are the same, and the curvature on that point is $\leq \kappa_{max}$, so no circular segment is used.

$$y_t^{\eta} = \sqrt{\frac{\pi}{\sigma}} \, S_f\left(\sqrt{\frac{(t\kappa_{max})^2}{\pi * \sigma}}\right), \qquad (4)$$

where C_f and S_f represent the Fresnel integrals, while κ_t^{η}, θ_t^{η}, x_t^{η}, and y_t^{η} indicate the curvature, angle, x-axis position, and y-axis position of the clothoid at a normalized segment length $t \in [0, 1]$, respectively.

A smooth turn starts and exits with transitions between straight lines and circular segments. However, for a turn with an angular difference α, only when the angle of the clothoid at maximum curvature (θ_{max}) is less than half of α, a circular segment of $\alpha - 2\theta_{max}$ is incorporated (Figure 4a). Otherwise, the turn does not need a circular segment (Figure 4b), and both clothoids (Equations 1–4) have a t equal to:

$$t = \frac{\sqrt{\alpha * \sigma}}{\kappa_{max}}.$$

For a left turn, the first clothoid segment uses a positive rate of curvature change, $\sigma = \sigma_{max}$, while for a right turn the negative value is used, $\sigma = -\sigma_{max}$. The sign of σ for the second clothoid segment in a sequence is always the opposite of that of the first clothoid.

This study introduces a variation of the standard clothoid by introducing a buffering distance D. This adjustment maintains the angle but alters the curvature and the x and y coordinates as described in the following equations:

$$\kappa_t^{\zeta} = \frac{t\kappa_{max}}{Dt\kappa_{max} + 1}$$
$$x_t^{\zeta} = x_t^{\eta} + D\sin(\theta_t^{\eta})$$
$$y_t^{\zeta} = y_t^{\eta} + D(1 - \cos(\theta_t^{\eta}))$$

Buffered clothoids ensure parallel paths at a distance D, thus minimizing overlap between swaths while maintaining continuity in curvature properties. These buffered clothoids can replace standard clothoids in smooth turns, as calculated using the same method (Figure 4).

Henceforth, this paper will refer to smooth turns as standard left/right turns if they use standard clothoids, while those employing buffered clothoids being designated as buffered left/right turns.

2.3 | Covering Field Headlands

Headlands consist of N concentric headland tracks, where each track is represented by a vector of points forming edges connected by direct lines, with the first and last points identical. A headland track cannot contain any self-intersection. The outermost headland track is the one nearest to the field border. Inner tracks are created by inwardly moving the outermost track by a distance corresponding to the robot's coverage width, W_C.

Before creating the inner headland tracks, the computation of the outermost one involves the inward displacement of each edge by a specific offset δ_j, being j the index of the edge. It is presupposed that edges are sufficiently large to prevent reduction to zero due to this displacement. The offset for each edge is calculated based on the maximum offsets at its corners, incorporating both start and end offsets (δ^{cs} and δ^{ce}). These offsets are subject to the robotic system parameters and the planners selected for each corner.

Once the offsets for each edge are determined, corner turns are computed. This entails considering the offsets and

planner parameters to ensure the robot's effective navigation of each turn, thereby covering the headlands efficiently while keeping the robot and implement within field borders.

2.4 | Corner Path Planning

For each corner in the field, a corner turn is independently planned from the rest of the field. Then, that corner turn depends only on the robot parameters and the geometry of the corner. A corner in a field is delineated by two successive edges, and characterized by three points on the xy-plane, C_1, C_2, and C_3. The corner angle, $\alpha \in (-\pi, \pi]$, represents the angular deviation between the two edges of the corner. A corner is deemed convex if $\alpha > 0$, and concave if $\alpha < 0$. The turn planning strategy diverges based on the corner's nature—convex or concave.

For convenience, the corner points are transformed by xy-shifts and a rotation to a local coordinates system where the middle point is located at $(0, 0)$, and the first edge of the corner is parallel to the x-axis. Note that this transformation ensures that distances and angles between the points of the corner are maintained. The transformed points of the corner are denoted as C_1', C_2', and C_3'. The border of the field near the first edge of the corner, after the transformation, is located at $y' = -\delta^{cs}$, parallel to the first edge, while the second edge parallels the second border edge at δ^{ce} distance. The computed path is transformed back to the xy-plane coordinate system using the inverse transformation, first rotating and then inverting the xy-shifts.

2.5 | Convex Corner Path Planning

2.5.1 | Convex C-Type and B-Type Corner Turns

The Convex C-type corner turn (Figure 5a) involves a single smooth left turn. Through the turn, the implement is continuously being used. On one hand, the time required to deactivate and activate the implement is saved. On the other hand, the turn has to be smoother when the implement is on, to avoid damaging the machinery.

This method has potential disadvantages, such as the creation of uncovered areas between swaths. To mitigate this, (Jeon et al. 2021) suggested buffering the inner circular segment for subsequent corner turns. This adjustment shifts the uncovered area outside the already covered territory.

Following the approach of (Jeon et al. 2021), a variation of the Convex C-type corner turn is proposed: the B-type corner turn (Figure 5b). In this variant, the left smooth turn is replaced by a buffered one, using buffered clothoids (Figure 4) with $D = i * W_C$, where D represents the buffered distance, and i is the number of headland swaths from the inner corner to the planned corner.
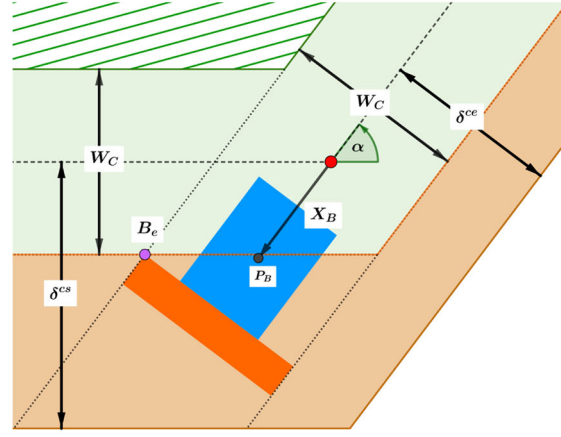
2.5.2 | Convex X-Type Corner

In the Convex X-type Corner strategy (Figure 6), the robot initially advances forward following the start headland swath a distance X_A, to P_A (Figure 6a). Then the implement is turned off
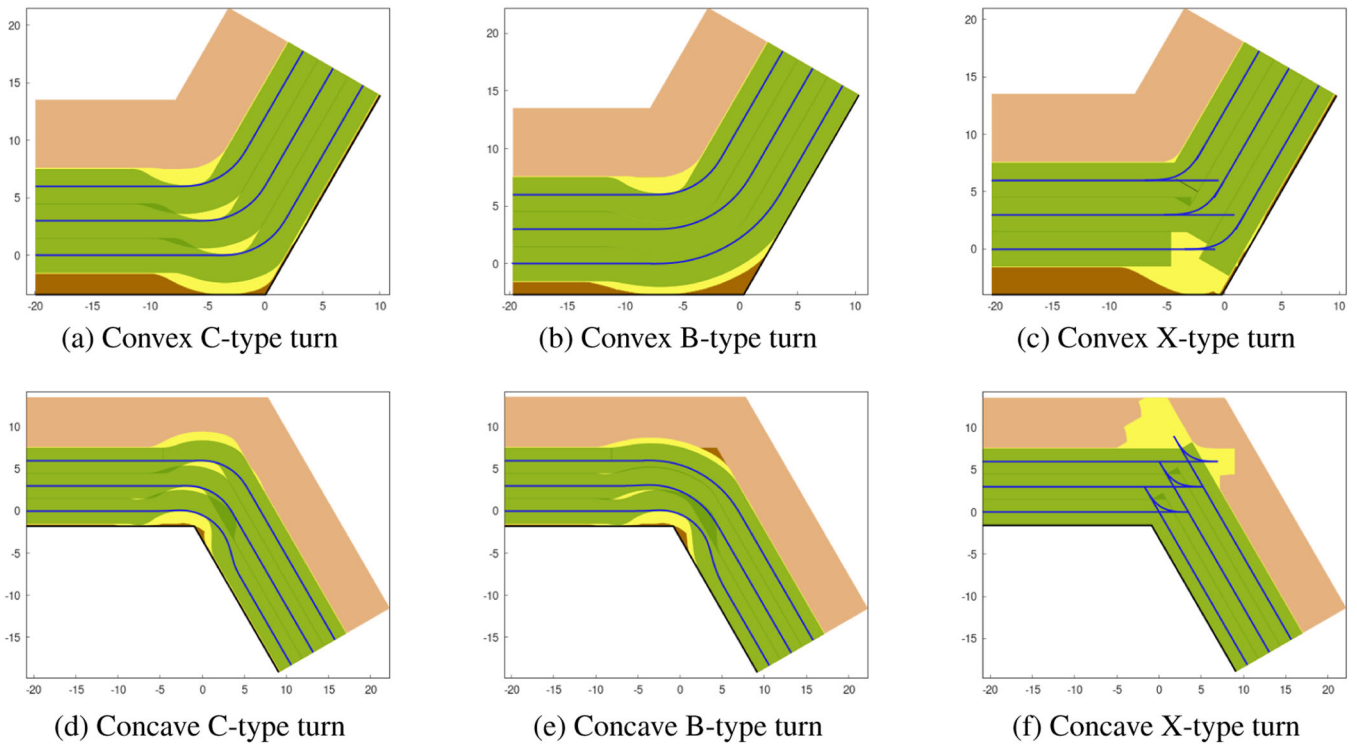
FIGURE 5 | Robot motions for corner convex turns, $\alpha = \pi/3$ (a–c), and concave turns, $\alpha = -\pi/3$ (d–f), using each type of planner for three headland tracks. Green area is the area covered. Yellow is the area traversed. Dark brown is the headland area, and light brown is the field area.
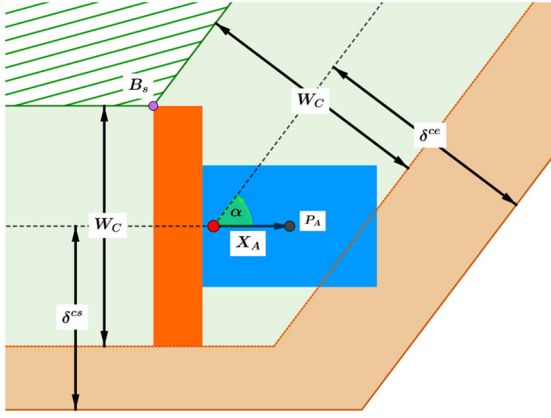
(a) Position of the robot at the start of the turn. The rear corner of the implement touches B_s to guarantee complete coverage of the start swath. At point P_A the robot turns off the implement.

(b) Position of the robot at the end of the turn. The front corner of the implement touches B_e. At point P_B the implement is turned on to continue covering the end swath.

FIGURE 6 | Convex X-type corner turn. The robot is represented in blue, and the implement in orange. The green area represents the covered part of headland swaths; the brown is the uncovered headland area; the striped green area is the mainland. α represents the angle between both swaths, W_I is the width of the implement, and δ^{cs} and δ^{ce} are the offset of the turn at the start and the end swaths. (a) Position of the robot at the start of the turn. The rear corner of the implement touches B_s to guarantee complete coverage of the start swath. At point P_A the robot turns off the implement. (b) Position of the robot at the end of the turn. The front corner of the implement touches B_e. At point P_B the implement is turned on to continue covering the end swath.

and the robot continues moving backward until the start of the forward-moving left turn. After the backward smooth turn (Figure 6b), the robot go backwards on the end headland swath a distance X_B, to P_B, turns on the implement, and ends in with forward movement to continue covering the end headland swath.

The region where the headland swaths intersect is subject to overlapping due to the robot traversing both paths. An area is only considered covered when the entire coverage area of the implement has passed over it. To reduce this overlap, given that the implement is mounted at the robot's rear, the variable X_A is selected to cover the start headland swath excluding its intersection with the end headland swath. In contrast, X_B is assigned to completely cover the end headland swath, including the overlapping region. Therefore, X_A is determined by the rear of the coverage area, while X_B is determined by its front part.

The values for X_A and X_B are calculated using the following equations:

$$X_A = C_b - \frac{W_C}{2} * \left(\frac{1}{|\sin \alpha|} - \frac{1}{|\tan \alpha|} \right), \tag{5}$$

$$X_B = C_f - \frac{W_C}{2} * \left(\frac{1}{|\sin \alpha|} + \frac{1}{|\tan \alpha|} \right). \tag{6}$$

While X_A and X_B depend on the coverage area of the implement, constrains using the robot physical dimensions are applied to prevent the robot from leaving the operational area (Figure 7). Specifically, $X_A \leq X_A^{\max}$ and $X_B \geq X_B^{\min}$, where:

$$X_A^{\max} = \frac{\delta^{ce}}{\sin \alpha} - \max\left(\frac{L_R}{2} + \left| \frac{W_R}{2 \tan \alpha} \right|, I_f + \left| \frac{W_I}{2 \tan \alpha} \right| \right)$$

$$X_B^{\min} = -\frac{\delta^{cs}}{\sin \alpha} + \min\left(\frac{-L_R}{2} + \left| \frac{W_R}{2 \tan \alpha} \right|, I_b + \left| \frac{W_I}{2 \tan \alpha} \right| \right).$$

If $X_A^{\max} < 0$ or $X_B^{\min} > 0$, the turn causes the robot to exceed the field's borders, requiring an increase in either δ^{cs} or δ^{ce}.

2.6 | Concave Corner Path Planning

2.6.1 | Concave C-Type and B-Type Corner Turns

The Concave C-type corner turn (Figures 5d and 8) is a sequence of three smooth turns, that includes a left turn up to an inflection angle γ_s, a subsequent right turn through an angle totaling $\alpha + \gamma_s + \gamma_e$, and a final left turn by an inflection angle γ_e.

The inflexion angles, γ_s and γ_e, prevent the robot from colliding with the corner of the field. To determine the inflexion angles that minimize the length of the planned corner turn, an exhaustive search is employed, exploring angles within the range of $[0, \frac{\pi}{2}]$ in increments of 0.0125π radians. During this search, a planned path is only valid if:

- The robot does not cross a line at $y = -\delta^{cs}$ while executing a left turn of angle γ_s.

- Similarly, it avoids crossing a line at $y = -\delta^{ce}$ during a left turn of angle γ_e, assuming that the robot is going backwards during the turn.

- The path maintains a minimum distance of half of the robotic system's width from the border corner.
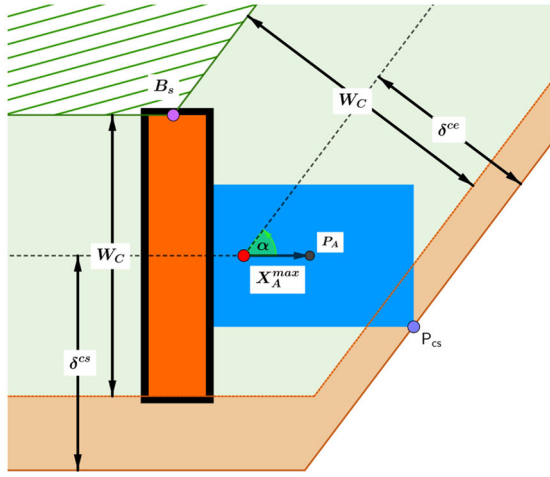
(a) The front of the robot touches the border of the field (P_{cs}), which limits the implement to completely cover the start swath.
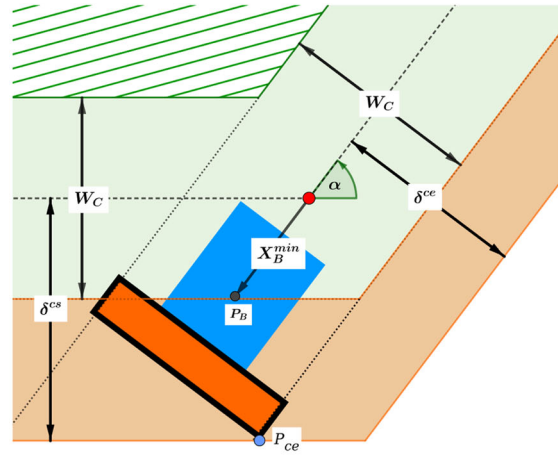
(b) The back of the robot touches the border of the field (P_{ce}), constraining the robot movement.

FIGURE 7 | Cases where the robot is physically constrained by the border of the field. The robotic system is represented as a blue box for the robot, a black box for the implement, and an orange box for the coverage area of the implement. α represents the angle between both swaths, W_C is the coverage width of the implement, and δ^{cs} and δ^{ce} are the offset of the turn at the start and the end swaths. (a) The front of the robot touches the border of the field (P_{cs}), which limits the implement to completely cover the start swath. (b) The back of the robot touches the border of the field (P_{ce}), constraining the robot movement.
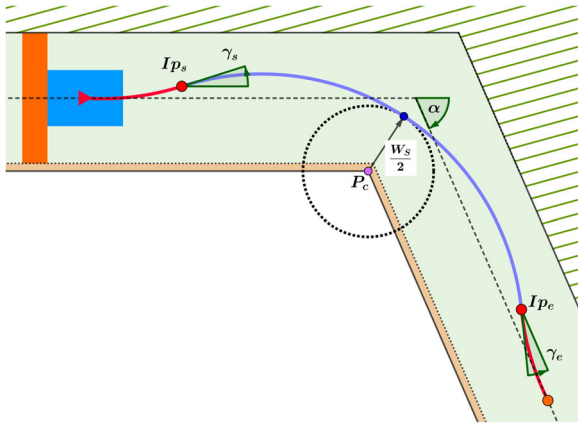
FIGURE 8 | Concave C-type turn made by two left turns (red lines), and one right turn (purple line). Green area is the area of the headland swaths, brown area is the area between the border and the headland swath, and the green striped area is the mainland. The border area has a width of δ^{cs} on the starting line, and δ^{ce} on the ending line. P_C is the corner of turn. The dotted circle around P_C, with radius $W_S/2$, represents the collision region of the corner with the robot. If the path enters into the dotted circle, the robot would collide with the border of the field.

As in the convex case, a variation of the Concave C-type corner turn is proposed, called Concave B-type corner turns (Figure 5e), using buffered turns instead.

2.6.2 | Concave X-Type Corner Turn

In a Concave X-type corner turn (Figures 5f and 9), the robot initially advances with its implement operational. This is

followed by the deactivation (lifting) of the implement at P_A and moves towards point P_{rs} (Figure 9a), either forward or in reverse. Subsequently, the robot performs a reverse left turn, proceeds to point P_{re} (Figure 9b) in either direction, reactivates the implement at P_B, and resumes forward motion.

The calculations for X_A and X_B in this scenario follow the same formulas as in the Convex X-type corner turn, specifically Equations (5) and (6). Unlike in the convex scenario, these variables are not bounded due to the lack of collision risk with the edges of the field.
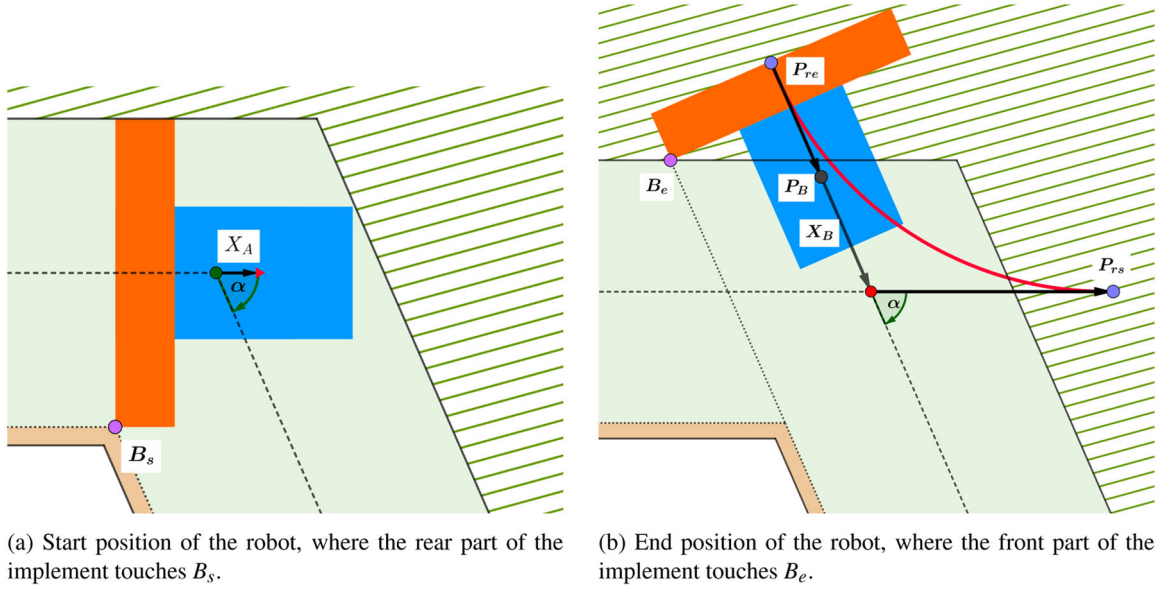
2.7 | Computing Edge Offset

To analyze the robot's required offsets during corner turns, a simplified path is used instead of the complete one, to reduce computations. The simplified path starts at (0, 0) with zero angle, involving a left turn (can be buffered turn), and ends at angle τ. While in convex turns $\tau = \alpha$, in concave turns τ has not the same value as α.

For each corner of the robotic system along the simplified path, the minimum y-value is computed. This minimum occurs when the robot's angle $\in [0, \tau]$. As the y-value function is convex for the defined range, employing the Bisection Method or any convex optimizer is effective for finding this minimum. The minimum of all the corners of the robotic system is used as the minimum offset required by the robot to prevent crossing the borders of the field.

For the calculation of offsets δ^{cs} and δ^{ce} on convex turns, a forward smooth turn is planned from angle 0 to α. For X-type corner turns, the maximum curvature of the turn is κ_{off}, while for C-type and B-type corner turns use κ_{on} as maximum curvature.

(a) Start position of the robot, where the rear part of the implement touches B_s.

(b) End position of the robot, where the front part of the implement touches B_e.

FIGURE 9 | Diagram of Concave X-type corner turn. The turn starts at P_A, turning off the implement. Then the robot continues until P_{rs}, does a smooth turn backwards until P_{re}, and follows forward to P_B, where the implement is turned on again. (a) Start position of the robot, where the rear part of the implement touches B_s. (b) End position of the robot, where the front part of the implement touches B_e.

Offsets for Concave C-type & B-type corner turns are calculated using the same method as the usual turn planner, an exhaustive search, with the path length as the cost function. During each iteration, δ^{cs} and δ^{ce} are computed for the respective combinations of γ_s and γ_e.

Regarding the offsets for the Concave X-type turn, both the start and end offsets are set to half the width of the robotic system, denoted as $\frac{W_S}{2}$. This ensures that the robot maintains a safe distance from field edges, preventing any part of the robot from extending beyond the field limits during the turning maneuver.

2.8 | Corner Turns on Inner Headland Rings

On Section 2.4, turns are planned for the outer headland ring, which is closer to the border. Usually, headlands have more than one headland rings. The computation of corner turns on inner headland rings are equivalent to the turns on outer headland rings, using modified start and end offsets, δ^{cs} and δ^{ce}:

$$\delta_i^{cs} = (i-1) * W_C + \delta_1^{cs}$$
$$\delta_j^{ce} = (j-1) * W_C + \delta_1^{ce}.$$

Being δ_i^{cs} and δ_j^{ce} the offsets of the start and end edge on the ith and jth headland ring, respectively. The values i and $j \in [1, N]$, being 1 the outer ring and N the total number of headland rings. Whenever the corner is made within the same headland ring, $i = j$. To change the headland ring on the corner, $i \neq j$.

2.9 | Cost Functions

Following the nomenclature on Section 2.4, a corner is defined by three points, C_1, C_2, and C_3. Adapting it to a corner with more than one headland tracks (Figure 10), the points of a corner in

the ith headland track are denoted as $C_1^{(i)}$, $C_2^{(i)}$, and $C_3^{(i)}$. Points $C_1^{(1)}$, $C_2^{(1)}$, and $C_3^{(1)}$ define the outer corner. The points on the border of the field are B_1, B_2, and B_3. The distance from B_1 to $C_1^{(i)}$ is δ_i^{cs}, and δ_i^{ce} from B_3 to $C_3^{(i)}$. The border of the mainland is defined by the points M_1, M_2 and M_3. Those points are placed parallel to the corner points, $\overrightarrow{C_1^{(i)}C_2^{(i)}} \| \overrightarrow{M_1 M_2}$ and $\overrightarrow{C_2^{(i)}C_3^{(i)}} \| \overrightarrow{M_2 M_3}$, and at a distance $|\overrightarrow{C_j^{(i)} M_j}| = W_C * (N - i + 0.5)$, for $i \in [1, N], j \in \{1, 3\}$, being N the number of headland swaths.

Additionally, to simplify the following explanation some functions and variables are used:

- $\text{Path}_\rho(C_1, C_2, C_3)$: returns the path made by the robot to drive from point C_1 to C_3, using the planner $\rho \in c, b, x$.

- $A_{cov}(\text{Path}_\rho(C_1, C_2, C_3))$: returns the region covered by the robot during the path $\text{Path}_\rho(C_1, C_2, C_3)$.

- $\text{Area}(a)$ returns the area of a polygon a.

- H: returns the region of the headland around the corner made by C_1, C_2 and C_3. This area is the polygon: $(M_1, M_2, M_3, B_3, B_2, B_1, M_1)$.

The choice of planner for each corner is dictated by the normalized sum of the cost functions: the path length and the uncovered area.

The path length cost function sums up the length of the turn path for each headland track corner, i.e. $f_L(\rho) = \sum_{i=1}^{N} |\text{Path}_\rho(C_1^{(i)}, C_2^{(i)}, C_3^{(i)})|$. Conversely, the cost function for uncovered area calculates the area that remains unattended by the robot after executing all the turns at the headland ring corners, i.e. $f_A(\rho) = \text{Area}(H - \bigcup_{i=1}^{N} A_{cov}(\text{Path}_\rho(C_1^{(i)}, C_2^{(i)}, C_3^{(i)})))$.

$\text{Path}_\rho(C_1, C_2, C_3)$ is composed of a forward movement from C_1 to C_1^*, then a turn that finishes at C_3^*, and then another forward
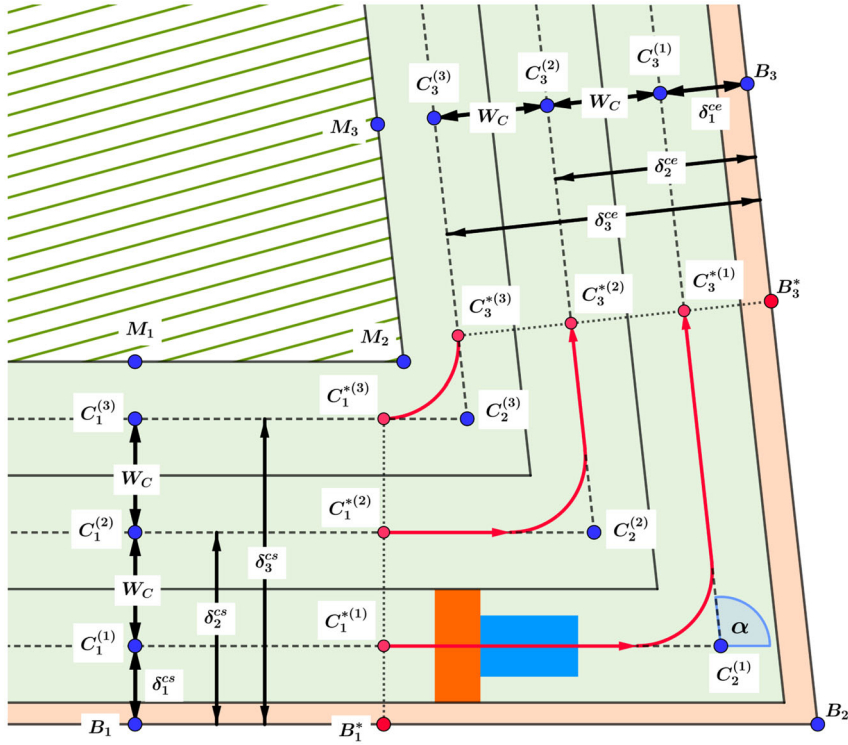
FIGURE 10 | Corner with three headland tracks. Points and distances are labeled following the nomenclature used in this work. The striped green area represents the mainland and the headland swaths are on green. Between the outer border and the headland swaths there is light brown area, which is a not-covered headland area to prevent the robot crossing the field borders. The blue and orange boxes are the robot and the implement, respectively.

movement until C_3. If C_1 is closer to C_2 than C_1^* or C_3 is closer to C_2 than C_3^*, then the turn is unfeasible because $\overrightarrow{C_1 C_1^*}$ or $\overrightarrow{C_3^* C_3}$ are not forward moves. Moreover, $\overrightarrow{C_1^{*(1)} C_1^{*(i)}} \perp \overrightarrow{B_1 B_2}$, and $\overrightarrow{C_3^{*(1)} C_3^{*(i)}} \perp \overrightarrow{B_2 B_3}$.

Both cost functions depend on the length of the edges of the field, $|\overrightarrow{B_1 B_2}|$ and $|\overrightarrow{B_2 B_3}|$. The vectors $\overrightarrow{C_1^{(i)} C_2^{(i)}}$ and $\overrightarrow{C_2^{(i)} C_3^{(i)}}$ change according to the length of those edges. The computation of the cost functions can be split between the cost of the forward movements and the cost of the turn, $f(\rho, B_1, B_2, B_3) = f^S(B_1, B_1^*) + f^T(\rho, B_1^*, B_2, B_3^*) + f^S(B_3^*, B_3)$, where f is the cost function, f^T is the cost function on the turn, and f^S on a straight forward movement. Specifically, for the path length and the uncovered area:

$$f_L^S(B_1, B_1^*) = N * \left| \overrightarrow{B_1 B_*^1} \right|$$

$$f_L^S(B_3^*, B_3) = N * \left| \overrightarrow{B_*^3 B_3} \right|$$

$$f_A^S(B_1, B_1^*) = (\delta_1^{cs} - W_C/2) * \left| \overrightarrow{B_1 B_*^1} \right|$$

$$f_A^S(B_3^*, B_3) = (\delta_1^{ce} - W_C/2) * \left| \overrightarrow{B_*^3 B_3} \right|$$

The function $f^T(\rho, B_1^*, B_2, B_3^*)$ does not depend on the position of B_1^*, B_2, and B_3^*, but only requires the angle α between the subsequent line segments, simplifying notation to $f^T(\rho, \alpha)$. This function has to be computed for each planner and angle, and its results can be cached to save computational resources.

To normalize the cost functions for all the angles and for a given pair of edges, the path length is divided by the length of the corners ($\sum_{i=1}^{N}(|\overrightarrow{C_1^{(i)} C_2^{(i)}}| + |\overrightarrow{C_2^{(i)} C_3^{(i)}}|)$), and the uncovered area by the area of the headland, $\text{Area}(H)$.

$$F_L(\rho, B_1, B_2, B_3) = \frac{f_L(\rho, B_1, B_2, B_3)}{\sum_{i=1}^{N}\left(|\overrightarrow{C_1^{(i)} C_2^{(i)}}| + |\overrightarrow{C_2^{(i)} C_3^{(i)}}|\right)}.$$

$$F_A(\rho, B_1, B_2, B_3) = \frac{f_A(\rho, B_1, B_2, B_3)}{\text{Area}(H)}$$

Note that $C_1^{(i)}, C_2^{(i)}, C_3^{(i)}$, and H depends on the edge lengths ($|\overrightarrow{B_1 B_2}|$ and $|\overrightarrow{B_2 B_3}|$) and the angle of the turn, α. A second normalization is made to scale both objective functions between $[0, 1]$ before adding them to the combined cost function, $G(\rho, \alpha)$.

$$G(\rho, \alpha) = \frac{F_A(\rho, \alpha) - \min(F_A)}{\max(F_A) - \min(F_A)} + \frac{F_L(\rho, \alpha) - \min(F_L)}{\max(F_L) - \min(F_L)}.$$

The optimal planner for a corner (given angle α and edge lengths) is the one that has the smallest combined cost, while being feasible to execute.

3 | Results

3.1 | Experiments

Several experiments were conducted to test the algorithms developed in this paper. The objective was to verify whether the

corner turn planners effectively plan the coverage of the headlands without crossing the field borders.

Field experiments were conducted using the Agbot robot equipped with an Amazone cultivator and seed drill (Figure 1). The specifications of the robotic system are given in Table 2. Computer code was implemented using C++ and the Fields2-Cover library (Mier et al. 2023). Matlab R2023a was used for visualization purposes. The laptop used for experiments was an MSI GF627RE with an Intel(R) Core(TM) i7-7700HQ CPU, running Ubuntu 22.04.5.

The metrics used for evaluating the algorithms' performance were:

- Absence of Collision Between the Robotic System and the Field Borders: Collisions cause the robot to exit the field area. The absence of collisions proved that the planners could execute turns without crossing the field borders.
- Path Length and Uncovered Headland Area: As previously explained, these metrics focused on maximizing headland coverage while minimizing operational time.

The tests involved three experiments:

- Simulated Planning in Single Corners: This experiment evaluated each corner planner presented in this work for individual corners. The tests concerned the influence of the number of headland tracks, the angle of the corner and the length of the edges on the election of the best corner planner. The experiment included three sub-experiments. The first studied the effect of the corner angle on the normalization process of the cost functions. The second compared the influence of edge lengths and number of headland tracks on the combined cost function. The third identified the best corner planner according to the number of headland tracks, the corner angle, and the edge lengths.
- Simulated Headland Coverage: In this experiment, 54 fields from the (Nilsson and Zhou 2020) benchmark were used to test the headland coverage path planners. Complete headland coverage was compared using a constant offset with the best planner for each corner, a single corner planner with the minimum offsets, and the best planner with minimum offset. The benefits of the proposed methods for headland coverage were assessed.
- Real-Life Experimentation: A custom field was laid out for real-life testing, designed to challenge navigation along convex and concave turns. The field, located near Oirlo, in the province of Limburg, the Netherlands, was part of a larger test field. The field borders were marked using tape, and the corners were identified using RTK GNSS. During the experiment, the cultivator was partly lifted to have it just touch the ground, leaving a visible trail while preventing equipment damage. The path was recorded using the robot on-board RTK-GNSS. From this, the total path length was derived. An unmanned aerial vehicle (UAV), with a camera and a RTK-GNSS, was used for tracking the worked area. The goal of this experiment was to assess the methodology's applicability, verifying that the robot can

indeed follow the headland coverage path without exiting the field.

In the second and third experiments, the mainland was assumed to be covered using adjacent parallel straight swaths, which was not detailed in this study.

3.2 | Simulated Planning in Single Corners

In the first experiment, the influence of the corner angle was studied on the normalization process of each cost function for each corner turn planner. Fixed values of three headland tracks and 100 m of length for both edges were used for this test. Those turns were evaluated on two cost functions: path length and uncovered headland area. Both cost functions were normalized using the method explained in Section 2.9.

Figure 11 shows the costs for turns with corner angle $\in (-\pi, \pi)$, and the normalization impact on cost functions, particularly for extreme corner angles. The left side of the figure illustrates the raw cost values, that is, path length and uncovered area, as a function of the corner angle. The right side demonstrates the effect of normalization on these cost functions. Negative angles denote concave turns, and positive angles indicate convex turns. Normalization significantly influences cost evaluation, particularly for angles substantially different from zero. For extreme cases near $-\pi$, normalization makes the large values more easily comparable.

As expected, in Figure 11, X-type turns had the longest path lengths, which was due to their complex maneuvering requirements. The uncovered area in concave X-type turns was almost negligible, since the required offset equals half the difference between the coverage width and the robot width. In this example, the convex B-type turns covered more headland area than convex C-type turns for $\alpha \in [0, 0.46\pi]$. Both outperformed convex X-type turns by covering more area owing to their smaller maximum curvature, which implied a smaller offset required for turning within the field limits. On the other hand, convex X-type turns covered more area for $\alpha \in [0.52\pi, 0.96\pi]$. In the range $\alpha \in (0.46\pi, 0.52\pi)$, C-type was the planner that left less area uncovered. Beyond this range, all three corner turns became unfeasible. The optimization results of the concave B-type exhibited noise due to optimization challenges. This can be particularly observed in the normalized cost functions of Figure 11 and suggests potential improvements to the optimizer for finding the inflection angles.

In the second experiment, corner planners were compared using the combined cost function, across different headland tracks, corner angles, and edge lengths. Moreover, this experiment showed that for certain values corner turns cannot be planned due to space constrains. This comparison was made for 1, 2, and 3 headland tracks and for 20, 60, and 200 m of edge lengths.

Figure 12 displays combined cost function values under these conditions, revealing preferences for different turn types based on the corner angle, edge length, and headland track count. The intersection points of cost function curves shifted with these parameters, indicating optimal planner choices in diverse scenarios.
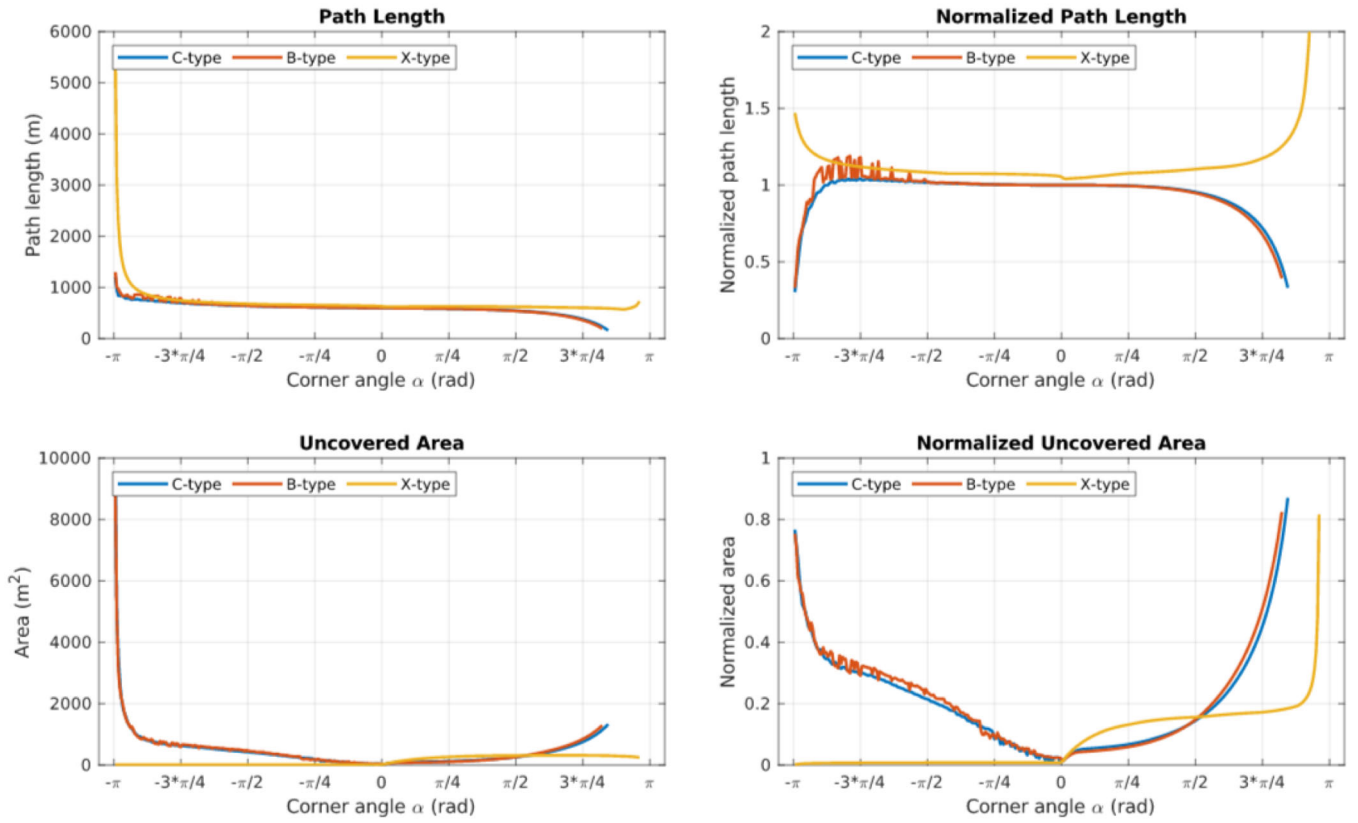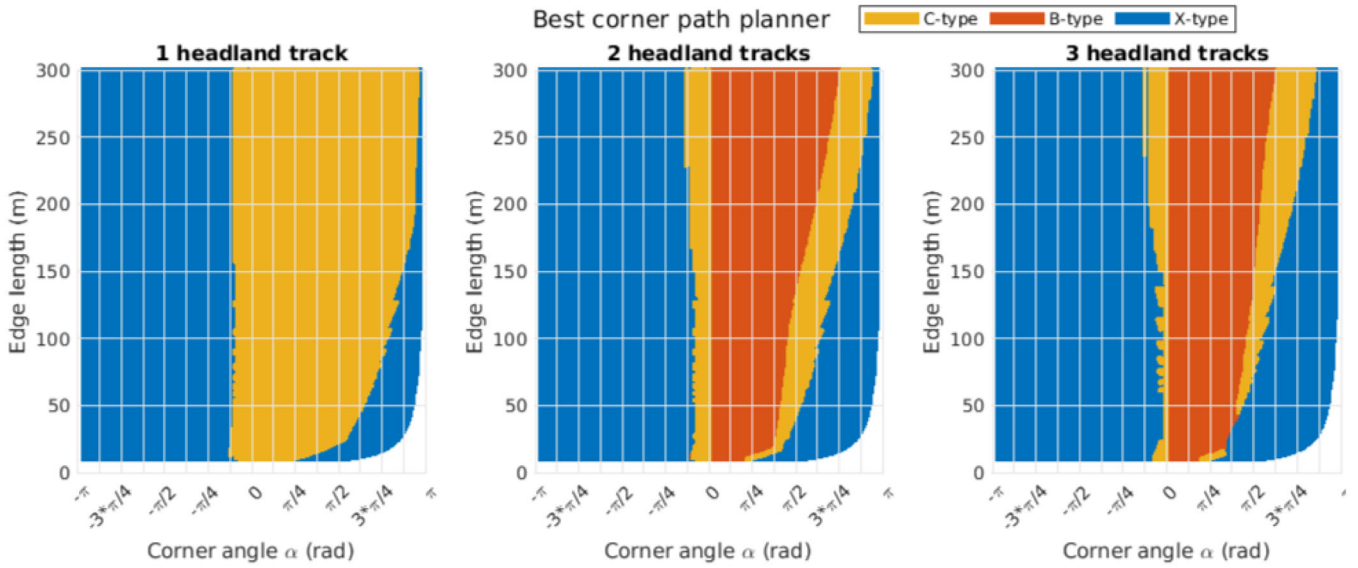
FIGURE 11 | Path length, uncovered area, and normalized cost functions comparison for corner turns (X-type, C-type, B-type) with 100-m edge lengths and three headland tracks.
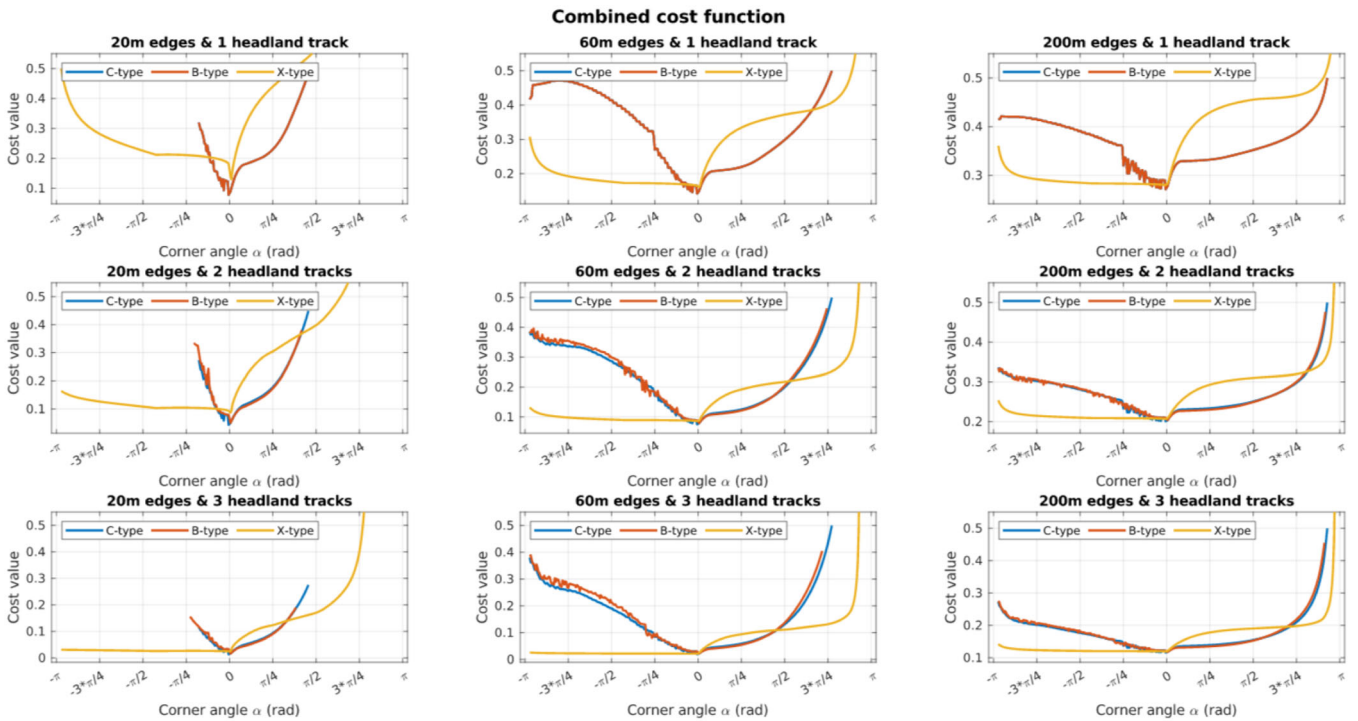
FIGURE 12 | Combined cost function evaluation across various corner angles, planners, edge lengths, and headland tracks.

FIGURE 13 | Optimal planner selection based on corner angle and edge length, indicating preferred turn types.

When only one headland track was used, B-type and C-type turns were similar, as clothoids are not buffered. In the case where edges were 20 m, some angles were unfeasible to make using the B/C-type turns due to the lack of space required. For convex turns, B-type was preferred to C-type from angle 0 to a point where both lines intersected. For bigger angles (after other line intersection between C-type and X-type), X-type was the best planner. This behavior can also be seen in Figure 11. These two inflexion points depend on the number of headland tracks and the length of the edges. Longer edges or less headland tracks moved the intersection point between C-type and X-type to bigger angles. For concave angles, there was only one intersection point between C-type and X-type. This intersection point was located near the angle 0, being preferred concave C-type only for small angles.

The third experiment (Figure 13) identified optimal planners based on corner angle and edge lengths. The results corroborated with those from Figures 11 and 12. X-type was often the preferred planner for concave corners, except at small negative angles. For convex corners, B-type was favored for smaller angles, while sharp convex corners suit X-type turns. Between the regions where B-type and X-type were preferred, C-type turns had a space in which it was the optimal planner. If the corner was too acute and edge lengths were short, none of the planners generated feasible paths.

The computing time required by each planner is shown in Figure 14. Each turn was computed 5 times to obtain the average of time it takes to plan it. Due to C-type and B-type turns produced similar results, the C-type planner is not represented to simplify the plot. Moreover, the edges length did not modify the computing times of the planners. As shown in Figure 14, for the same planner, the number of headland swaths proportionally increased the computing time, while for the same convexity, the corner angle did not affect it. Comparing the planners, the concave B-type planner is 10^5 times slower than the other turn planners because of its optimization process.
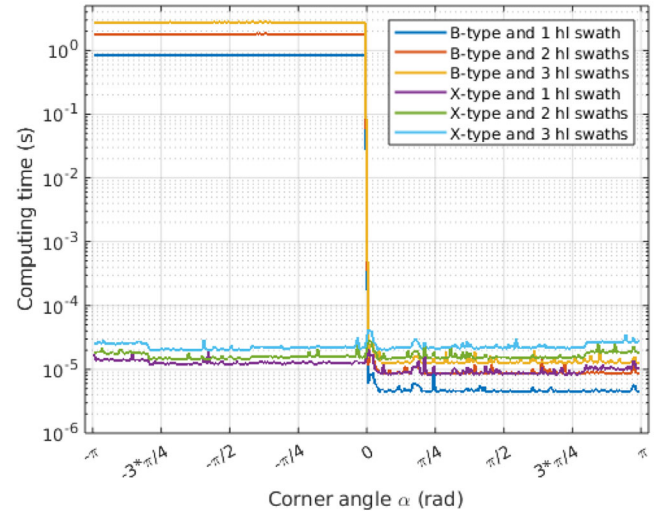
FIGURE 14 | Computing time required by the turn planners to compute a turn with swaths length of 200m, according to the planner used and the number of headland swaths. *y*-axis is in logarithm scale.

3.3 | Simulated Headland Coverage

Despite a corner path was planned using the geometric properties of the corner instead of the whole field boundary, the yield of the field was affected by all the corner paths planned.

Figure 15 showcases a field from the benchmark (Nilsson and Zhou 2020), illustrating the impact of planner choice on each corner. The field on Figure 15 was down-scaled to 1 ha for visualization purposes. The path demonstrated various turn types, with the coverage and uncovered areas distinctly marked. Starting at the bottom left corner, going in clockwise order from in-to-out order, the path did three B-type turns, followed by three X-type turns. This visualization aids in understanding the practical implications of different planners.

In this experiment the covered area was compared for complete fields, for three different cases:

- Constant offset. The best corner planner was chosen for each corner, but the border offsets had a constant value equal to $\delta_j = I_L$. This value was used as a safety measure to guarantee that the robot did not cross the borders.
- Single corner path planner (C-type, B-type, and X-type). Only one corner planner was used for all the corners. Border offsets were computed to be the minimum required to adhere to field borders.
- Proposed approach. The best corner planners were used, computing the minimum border offset required.

This comparison allowed to analyze the benefits of each improvement presented on this work, according to the percentage of covered area of the field.

Results of this comparison are shown on Table 3. The approach with constant offsets had the worst coverage values, as the constant safety distance left more area uncovered near the borders. When only one corner planner was used, coverage results depended on the field geometry, being the B-type corner planner the one with best maximum and mean coverage percentages. Note that the maximum coverage for the B-type planner was equal to the maximum coverage for the proposed
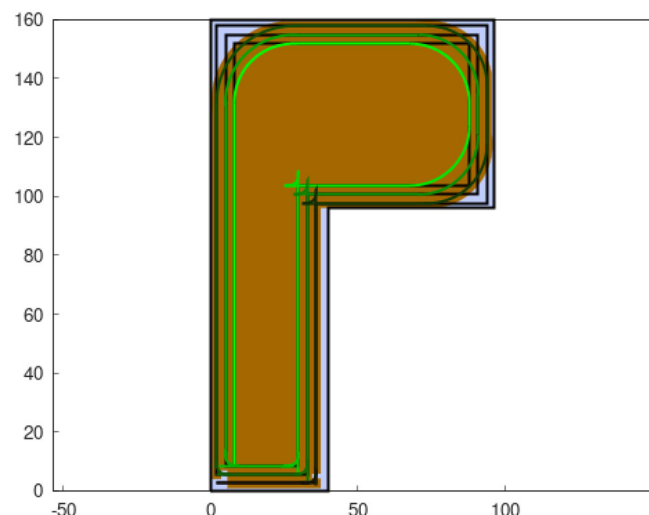
FIGURE 15 | Field ELE_A from (Nilsson and Zhou 2020), scaled to 1 ha, showing the coverage path of the headlands with marked covered (brown) and uncovered areas (light blue). The path color is light green at the beginning and gets darker in each new segment.

solution. This result was obtained for a square field, on which the B-type turn allowed the robot to approach field borders smoothly, requiring less extra space for the border offsets. Finally, our proposed approach obtained the best maximum (99.05%), mean (97.29%), and minimum (95.21%) coverage over the other approaches compared. In comparison, our approach was able to cover **2.56%** more field area than the constant offset approach.

These results confirmed the proposed approach behavior in simulations, maximizing the total covered area of the agricultural fields while observing their borders.

3.4 | Real-Life Experimentation

The third experiment was conducted to assess the proposed methodology's applicability in real life. The Agbot robot and the Amazone implement (Figure 1) were instructed to follow a headland coverage path plan. Owing to spatial limitations, the headland path comprised only a single track. A visual comparison was performed between the reference planned path and the path executed by the robot.

The experiment was conducted on June 26, 2023 under sunny and windy conditions. Figure 16 illustrates the experiment's outcomes. Due to the wind, the tape to mark the borders of the field bent inward along some edges. Except for three segments, the robot was able to follow the corner turns planned autonomously. Twice, the cultivator got tangled with the inward bent tape (green path in Figure 16). The third time, the human operator manually steered the robot out of the field (yellow path in Figure 16); this was due to a miscommunication about the size of the complete experiment. All autonomous maneuvers along the corners were successful, though. The robot successfully navigated a total path of 506.6 m without exiting the field borders, as shown by the buffered path representation in Figure 16.

4 | Conclusions and Future Work

In this paper, we have introduced a headland coverage path planning approach, focusing on maneuvers along the field borders. First, three types of continuous curvature turn planners were developed for convex and concave headland corners. These corner planners employ clothoids for generating smooth transitions between intersecting lines, a technique notably used in road alignment but rarely applied in agricultural path planning. Then, a new method was presented to quantify and correct the distance that a robot requires to perform a corner turn.

TABLE 3 | Coverage area comparison on the (Nilsson and Zhou 2020) benchmark with three headland tracks. Values are expressed as a percentage of covered area divided by the total area of the field.

	Const offset	C-type	B-type	X-type	Proposed approach
Max	96.62%	98.71%	**99.05%**	97.98%	**99.05%**
Mean	94.73%	96.88%	97.01%	95.76%	**97.29%**
Min	92.89%	93.24%	92.80%	94.35%	**95.21%**

Note: The bold values are the best results of each row.
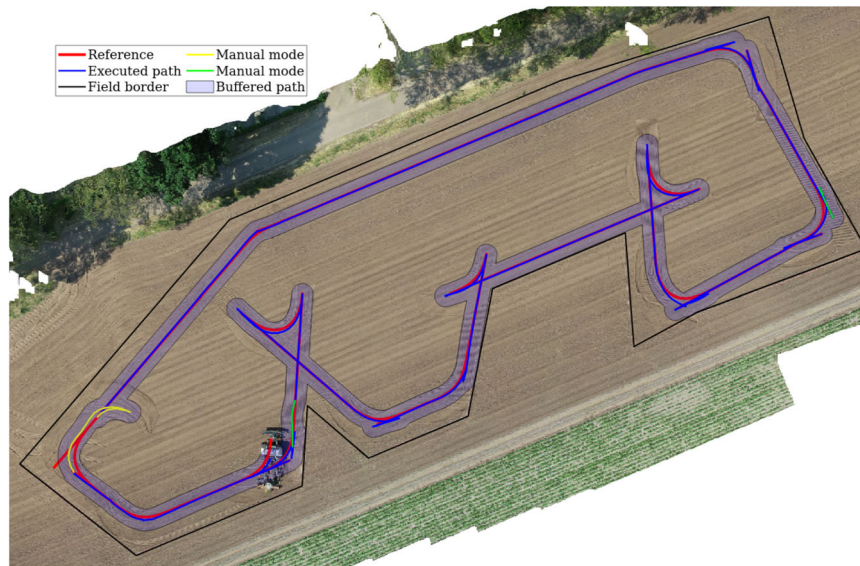
FIGURE 16 | Drone image of the field experiment, showing planned and actual robot paths. The path of the robot was buffered by half of its width to verify that the robot remained inside the field.

The method stands out for its potential to ensure the robot's confinement within field borders, especially with larger implements, by calculating a safety offset for each turn. This feature is critical in agricultural operations to prevent damage to crops and borders. Moreover, a selection mechanism for turn planners was explored, considering the area uncovered and the traveled distance as objective functions. Tests conducted with a coverage path planning benchmark and real-field trials using an autonomous robot demonstrated the efficacy of the proposed approach.

In contrast to previous literature, this work considered the dimensions of the robotic system to compute where field limits were trespassed, and offered a method to correct it. Though maximizing field coverage improves yield, some country regulations may promote or require fixed offsets near certain obstacles, i.e. ditches, limiting the benefits of our approach.

The test to measure the planners performance indicates that field size does not modify the computing time of the headland path, only the number of headland tracks and the concave C-type and B-type turns. Despite C-type and B-type planners for concave corners have a slow computing process—requiring seconds to compute—it is still manageable on real-time environments. Selecting faster optimizer for these planners is a challenge that will be tackle in future works.

Field experiments show how the proposed offline path planning approach behaves in real-world agricultural settings with a commercial robot and implement. Others components from the robotic system, such as navigation and control, are out of the scope of this study. Future research could assess the complete robotic system—combining path planning with the robot control and navigation system. This would give the opportunity to address other challenges such as wet soil, unexpected obstacles, and imprecise global localization.

The main limitation of the proposed approach applies to corners with short edges, where the robot does not have enough space to turn safely. Future research involves research on this topic, planning the headland coverage path for corners with short edges or fields with smooth edges. Moreover, corner path planners presented in this paper use a fixed maximum curvature to plan the corner turns. Smaller maximum curvature produces smoother turns, reducing the border offset required. An advanced approach would modify the maximum curvature of sections of the turn dynamically, to further minimize the area uncovered and the path length.

Following our commitment with the open-source community, the methods implemented for this paper will be provided on the next major release of the Fields2Cover library (version 3.0.0) (Mier et al. 2023).

Data Availability Statement

The data that support the findings will be available in Fields2Cover at https://github.com/Fields2Cover/Fields2Cover following an embargo from the date of publication to allow for commercialization of research findings.

References

Baykal, O., E. Tari, Z. Çoşkun, and M. Şahin. 1997. "New Transition Curve Joining Two Straight Lines." *Journal of Transportation Engineering* 123, no. 5: 337–345. https://doi.org/10.1061/(ASCE)0733-947X(1997)123:5(337).

Bochtis, D., and S. Vougioukas. 2008. "Minimising the Non-Working Distance Travelled by Machines Operating in a Headland Field Pattern." *Biosystems Engineering* 101, no. 1: 1–12. https://doi.org/10.1016/j.biosystemseng.2008.06.008.

Dubins, L. E. 1957. "On Curves of Minimal Length With a Constraint on Average Curvature, and With Prescribed Initial and Terminal Positions and Tangents." *American Journal of Mathematics* 79, no. 3: 497–516. https://doi.org/10.2307/2372560.

Fraichard, T., and A. Scheuer. 2004. "From Reeds and Shepp's to Continuous-Curvature Paths." *IEEE Transactions on Robotics* 20, no. 6: 1025–1035. https://doi.org/10.1109/TRO.2004.833789.

Höffmann, M., S. Patel, and C. Büskens. 2022. "Weight-Optimized Nurbs Curves: Headland Paths for Nonholonomic Field Robots." In *2022 8th International Conference on Automation, Robotics and Applications (ICARA)*, 81–85. IEEE. https://doi.org/10.1109/ICARA55094.2022.9738525.

Höffmann, M., S. Patel, and C. Büskens. 2023a. "Optimal Coverage Path Planning for Agricultural Vehicles With Curvature Constraints." *Agriculture* 13, no. 11: 2112. https://doi.org/10.3390/agriculture13112112.

Höffmann, M., S. Patel, and C. Büskens. 2023b. "Optimal Guidance Track Generation for Precision Agriculture: A Review of Coverage Path Planning Techniques." *Journal of Field Robotics* 41: 823. https://doi.org/10.1002/rob.22286.

Jeon, C.-W., H.-J. Kim, C. Yun, X. Han, and J. H. Kim. 2021. "Design and Validation Testing of a Complete Paddy Field-Coverage Path Planner for a Fully Autonomous Tillage Tractor." *Biosystems Engineering* 208: 79–97. https://doi.org/10.1016/j.biosystemseng.2021.05.008.

Mier, G., J. Valente, and S. de Bruin. 2023. "Fields2cover: An Open-Source Coverage Path Planning Library for Unmanned Agricultural Vehicles." *IEEE Robotics and Automation Letters* 8, no. 4: 2166–2172. https://doi.org/10.1109/LRA.2023.3248439.

Nilsson, R. S., and K. Zhou. 2020. "Method and Bench-Marking Framework for Coverage Path Planning in Arable Farming." *Biosystems Engineering* 198: 248–265. https://doi.org/10.1016/j.biosystemseng.2020.08.007.

Nobari, O., A. Nobari, and R. Eslamipoor. 2019. "Optimal Point-to-Point Path Planning of Manipulator by Using Vibration Damping Optimization Algorithm and Game Theory Method." *Journal of Testing and Evaluation* 47, no. 4: 2867–2888. https://doi.org/10.1520/JTE20180332.

Nørremark, M., R. S. Nilsson, and C. A. G. Sørensen. 2022. "In-Field Route Planning Optimisation and Performance Indicators of Grain Harvest Operations." *Agronomy* 12, no. 5: 1151. https://doi.org/10.3390/agronomy12051151.

Oliveira, L. F., A. P. Moreira, and M. F. Silva. 2021. "Advances in Agriculture Robotics: A State-of-the-Art Review and Challenges Ahead." *Robotics* 10, no. 2: 52. https://doi.org/10.3390/robotics10020052.

Paraforos, D. S., R. Hübner, and H. W. Griepentrog. 2018. "Automatic Determination of Headland Turning From Auto-Steering Position Data for Minimising the Infield Non-Working Time." *Computers and electronics in agriculture* 152: 393–400. https://doi.org/10.1016/j.compag.2018.07.035.

PourArab, D., M. Spisser, and C. Essert. 2023. "Complete Coverage Path Planning for Wheeled Agricultural Robots." *Journal of Field Robotics* 40, no. 6: 1460–1503. https://doi.org/10.1002/rob.22187.

Rahman, M. M., K. Ishii, and N. Noguchi. 2019. "Optimum Harvesting Area of Convex and Concave Polygon Field for Path Planning of Robot Combine Harvester." *Intelligent Service Robotics* 12, no. 2: 167–179. https://doi.org/10.1007/s11370-018-00273-4.

Reeds, J., and L. Shepp. 1990. "Optimal Paths for a Car That Goes Both Forwards and Backwards." *Pacific Journal of Mathematics* 145, no. 2: 367–393. https://doi.org/10.2140/pjm.1990.145.367.

Sabelhaus, D., F. Röben, L. P. M. zu Helligen, and P. S. Lammers. 2013. "Using Continuous-Curvature Paths to Generate Feasible Headland Turn Manoeuvres." *Biosystems Engineering* 116, no. 4: 399–409. https://doi.org/10.1016/j.biosystemseng.2013.08.012.

Spekken, M., and S. de Bruin. 2013. "Optimized Routing on Agricultural Fields by Minimizing Maneuvering and Servicing Time." *Precision agriculture* 14: 224–244. https://doi.org/10.1007/s11119-012-9290-5.

Spekken, M., J. P. Molin, and T. L. Romanelli. 2015. "Cost of Boundary Manoeuvres in Sugarcane Production." *Biosystems Engineering* 129: 112–126. https://doi.org/10.1016/j.biosystemseng.2014.09.007.

Trendafilov, K., G. Tihanov, V. Stoykova, and G. Shivacheva. 2023. "Algorithm for Optimizing the Movement of a Mountedmachine-Tractor Unit in the Headland of an Irregularly Shaped Field." *INMATEH-Agricultural Engineering* 70, no. 2: 320. https://doi.org/10.35633/inmateh-70-31.